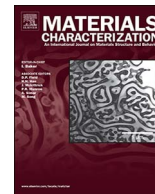




ELSEVIER

Contents lists available at ScienceDirect

Materials Characterization

journal homepage: www.elsevier.com/locate/matchar

Evolution of the microstructure during annealing of ultrafine-grained Ni with different Mo contents

Garima Kapoor^a, Yi Huang^b, V. Subramanya Sarma^c, Terence G. Langdon^b, Jenő Gubicza^{a,*}

^a Department of Materials Physics, Eötvös Loránd University, P.O.B.32, Budapest H-1518, Hungary

^b Materials Research Group, Faculty of Engineering and the Environment, University of Southampton, Southampton SO17 1BJ, UK

^c Department of Metallurgical and Materials Engineering, Indian Institute of Technology Madras, Chennai 600036, India

ARTICLE INFO

Keywords:

High-pressure torsion
Ni-Mo alloys
Dislocation density
Recovery
Recrystallization

ABSTRACT

Research was undertaken to evaluate the thermal stability of ultrafine-grained (UFG) Ni alloys with two different molybdenum (Mo) contents. The UFG microstructures in Ni samples with low (~0.28 at.%) and high (~5.04 at.%) Mo concentrations were achieved by the consecutive application of cryorolling and high-pressure torsion (HPT). The evolution of the microstructure during annealing up to ~1000 K was studied by differential scanning calorimetry (DSC) at the peripheral regions of the disks processed by 20 turns of HPT. The grain size and the fraction of low-angle grain boundaries (LAGBs) were monitored by electron backscatter diffraction while the dislocation density was determined by X-ray line profile analysis as a function of temperature. It was found that the recovery of the UFG microstructures started at ~400 K irrespective of the Mo content but recrystallization occurred at a much higher temperature for the Ni alloy with higher Mo content. During recovery, the LAGB fraction increased due to the arrangement of dislocations into low energy configurations. In the recrystallization process, the fraction of LAGBs decreased. After annealing up to ~1000 K, the grain size remained much smaller for the sample with higher Mo concentration. Moreover, the larger Mo content yielded a separation of recovery and recrystallization processes in the DSC thermogram. It is concluded that the higher Mo concentration has a more pronounced hindering effect on recrystallization than on recovery.

1. Introduction

In recent years, severe plastic deformation (SPD) techniques have emerged as attractive and promising routes for the production of bulk ultrafine-grained (UFG) materials [1–3]. SPD-processed UFG materials with contamination- and porosity-free microstructures exhibit improved mechanical behavior, such as high yield strength and ultimate tensile strength values. High pressure torsion (HPT) has been considered as one of the most effective SPD methods which applies extremely large strain everywhere apart from the centers of the HPT-processed disks [4]. This large shear strain and the high applied pressure not only cause significant grain refinement but also introduce a substantial dislocation density which leads to an enhanced mechanical strength [5].

The stability of UFG microstructures is a prerequisite of their reliable operation in practical applications. When grain growth occurs the improved strength of UFG materials deteriorates and therefore a study of the microstructural stability is necessary for the commercialization of these materials. The recovery and recrystallization behaviors of UFG materials are usually investigated by differential scanning

calorimetry (DSC) combined with direct or indirect observations of the microstructure [6–9]. Former studies revealed that for SPD-processed pure metals and dilute alloys the recovery of dislocation structure and recrystallization could not be separated in the thermograms since they occur in a single exothermic DSC peak [10–17]. The temperature of the peak maximum depends on the method of SPD processing, the imposed strain and the heating rate. However, its value is usually between $\sim 0.3\text{--}0.4 \times T_m$, where T_m is the melting point in Kelvin degrees [5]. It was also shown that the activation energy of recovery/recrystallization is usually about $0.5 \pm 0.1 \times Q_{\text{self}}$ where Q_{self} is the activation energy of self-diffusion, irrespective of the type of material and the processing method [18–21]. The observed values of the activation energies suggest that recovery and recrystallization are mainly controlled by diffusion along grain boundaries and dislocations. It is noted that for 4N and 4N8 purity Ni samples processed by HPT, an additional small DSC peak was observed at the homologous temperature of ~0.24 which corresponds to the annihilation of single and double vacancies [22]. However, the majority of reported DSC experiments do not show this vacancy peak. At the same time, for solid solutions with high solute content and precipitate hardened alloys, two

* Corresponding author.

E-mail address: jeno.gubicza@tk.elte.hu (J. Gubicza).

<http://dx.doi.org/10.1016/j.matchar.2017.05.034>

Received 16 April 2017; Received in revised form 17 May 2017; Accepted 26 May 2017

Available online 27 May 2017

1044-5803/ © 2017 Elsevier Inc. All rights reserved.

exothermic peaks were often observed [23,24]. The first peak is related to recovery while the second peak corresponds to recrystallization and grain growth. This separation of recovery and recrystallization is attributed to the segregation of alloying elements and/or the formation of precipitates at grain boundaries. Then, these act as obstacles against grain boundary migration, thereby hindering recrystallization and grain growth. The activation energy for the first “recovery” peak is usually smaller than that determined for the second “recrystallization” peak. Despite the numerous reports on DSC studies of SPD-processed metallic materials, systematic studies on the influence of strong alloying on the thermal stability of the defect structure and the grain size have not been performed to date.

In a recently published study [25], the dislocation density and the grain size in HPT processed Ni-Mo alloys with low (~0.28 at.%) and high (~5.04 at.%) Mo concentrations were compared. It was found that Mo alloying has a significant effect on the evolution of microstructure during HPT. However, no study has been documented to examine the thermal stability of UFG Ni-Mo alloys, despite their considerable practical applications. For instance, Ni-Mo alloys can be used as hard coating materials due to their high hardness, wear and corrosion resistances [26]. These alloys are also applicable as substrate material for superconducting coatings and they are used as catalysts in the production of hydrogen. The Ni-Mo substrates for superconducting coatings produced by severe cold rolling and subsequent annealing provide the extremely sharp cube texture which is required for epitaxial coatings [27]. Ni-Mo alloys, either in the form of catalyst coating or unsupported nanopowder, show high activity and long-term stability as hydrogen evolution reaction catalysts under alkaline conditions [28–30]. Accordingly, the present study examines the influence of Mo alloying on the thermal stability of HPT-processed UFG Ni alloys. For this purpose, two alloys with low (~0.28 at.%) and high (~5.04 at.%) Mo concentrations were processed by HPT and then annealed in DSC. The evolution of microstructural parameters, including grain size and dislocation density, were investigated as a function of the annealing temperature and then correlated to the evolved DSC peaks.

2. Experimental Materials and Procedures

2.1. Processing of UFG Ni-Mo Alloys

Two Ni alloys with low (~0.28 at.%) and high (~5.04 at.%) Mo contents were investigated and hereafter they are referred to as Low-Mo and High-Mo alloys, respectively. The chemical composition of the Low-Mo material was 98.29% Ni, 0.28% Mo, 0.84% Al, 0.34% Si and 0.25% Fe (in at.%) [25]. For the High-Mo alloy, the concentrations of chemical elements were 93.70% Ni, 5.04% Mo, 1.08% Al, 0.05% Si and 0.13% Fe (in at.%) [25]. It is readily apparent that the most significant difference between the chemical compositions of the two materials was the much higher Mo content in the material labelled High-Mo.

Both alloys were prepared by induction melting and casting into a Cu-mould. The as-cast ingots, having diameters of ~32 mm, were hot rolled at 1100 °C to a thickness of ~13 mm. The hot rolled samples were subjected to a two-step combined SPD process. In the first step, small strips were cut from the hot rolled materials and cryorolled at liquid nitrogen temperature (LNT). During cryorolling, the thickness decreased from ~13 mm to ~3 mm in multiple passes with a thickness reduction of ~5% per pass. After each cryorolling pass, the strips were cooled again to LNT. From the plates obtained after cryorolling, discs were prepared with diameters of 10 mm and thicknesses of 1 mm by Electric Discharge Machining (EDM). These samples were then processed by HPT technique under quasi-constrained conditions [31] with an applied pressure of 6.0 GPa and a rotation speed of 1 rpm at room temperature (RT) for 20 turns.

2.2. Differential Scanning Calorimetry

Differential scanning calorimetry (DSC) was used to investigate the thermal stability of the phase composition and the microstructure at the peripheral regions of the HPT-processed specimens. It was shown recently that for both Mo contents the microstructure achieved a saturation state between the half-radius and the periphery of the disks processed for 20 turns of HPT [25]. Therefore, for the DSC studies, small samples were cut from these regions of the disks. The DSC experiments were performed using a Perkin Elmer (DSC2) calorimeter at a heating rate of 40 K/min under an Ar atmosphere. The upper limit of temperature for this calorimeter was 1000 K.

2.3. Microstructure From EBSD

In order to study the microstructure evolution during annealing, samples were heated up to the characteristic temperatures of the thermograms and then quenched to RT. The microstructures of the HPT-processed and annealed Ni alloys were characterized by electron backscatter diffraction (EBSD) using an FEI Quanta 3D scanning electron microscope (SEM). Before EBSD, the surfaces of the samples were first mechanically polished with 600, 1200, 2500 and 4000 grit SiC abrasive papers and then the surface treatment was continued by polishing with a colloidal silica suspension (OP-S) having a particle size of 1 µm. Finally, electropolishing of the surfaces was conducted at 28 V and 1 A using an electrolyte with a composition of 70% ethanol, 20% glycerine and 10% perchloric acid (in vol%). The step size of the EBSD scans varied between ~10 and ~50 nm and larger step sizes were used for the samples exhibiting coarser microstructures. The EBSD data were evaluated using the Orientation Imaging Microscopy (OIM) software. The average grain sizes and the fractions of the low and high-angle grain boundaries (LAGBs and HAGBs) were determined from the EBSD images. The grains were considered as the regions in the EBSD images bounded by high-angle grain boundaries (HAGBs) having misorientations higher than 15°. The number-averaged grain size values were then determined for the HPT-processed and the annealed samples. The LAGBs were defined as the boundaries with misorientations between 2 and 15°.

The distortions inside the grains were analysed using Kernel Average Misorientation (KAM) maps prepared by the OIM software. In this evaluation process, a local misorientation angle value was assigned to each pixel which was determined as the average misorientation between the studied central pixel and all pixels at the perimeter of the kernel around the investigated pixel. The radii of the kernels were maintained the same (~50 nm) for all images even if their pixel sizes were smaller in order to make their KAM maps comparable.

2.4. Characterization of Microstructure by X-ray Diffraction

The phase composition and the average lattice parameter values for the Ni alloys were determined by X-ray diffraction (XRD) using a Philips Xpert Θ - 2Θ powder diffractometer operating at 40 kV and 30 mA with CuK α radiation (wavelength: $\lambda = 0.15418$ nm). The measured XRD patterns indicated that all samples had face-centered cubic (fcc) structure. The average lattice parameter was determined from the diffraction peak positions using the Nelson–Riley method [32].

The defect structure of the SPD-processed Ni alloys were studied by X-ray line profile analysis (XLPA). The XRD patterns were measured by a high-resolution diffractometer (Rigaku) with CuK α_1 radiation (wavelength: $\lambda = 0.15406$ nm). The Debye–Scherrer diffraction rings were detected by two dimensional imaging plates and the line profiles were determined as the intensity distributions perpendicular to the rings obtained by integrating the two dimensional intensity distributions along the rings. The evaluation of the patterns was carried out by the Convolutional Multiple Whole Profile (CMWP) fitting method [33]. In this procedure, the experimental diffraction pattern is fitted by the sum

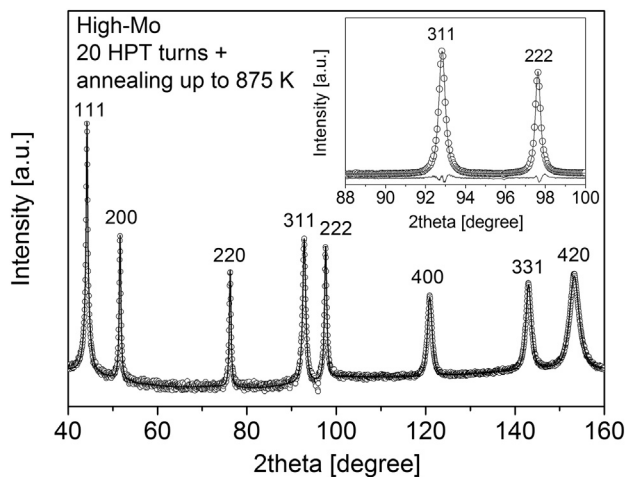


Fig. 1. CMWP fitting on the diffraction pattern taken on the High-Mo alloy processed by 20 turns of HPT and heated up to ~ 875 K. The open circles and the solid line represent the measured and the fitted patterns, respectively. The intensity is plotted in logarithmic scale. The inset shows reflections 311 and 222 with higher magnification and linear intensity scale. The difference between the measured and fitted diffractograms is shown at the bottom of the inset.

of a background spline and the convolution of the instrumental pattern and the theoretical line profiles related to crystallite size, dislocations and planar faults. The theoretical line profile functions used in this fitting procedure were based on a model of the microstructure where the crystallites have spherical shape and a log-normal size distribution. As an example, Fig. 1 shows the CMWP fitting for the HPT-processed High-Mo sample annealed up to 875 K. The open circles and the solid line represent the measured and fitted intensity profiles, respectively. The difference between the measured and the fitted diffractograms was practically zero, thus indicating a good fitting of the measured diffractogram by the theoretical pattern. The following two parameters of the dislocation structure were determined by the CMWP fitting procedure: the average dislocation density (ρ) and the dislocation arrangement parameter M . The value of the parameter M reflects the arrangement of dislocations. Thus, a smaller value of M relates to a more shielded strain field of dislocations and the arrangement of dislocations into low energy configurations, such as LAGBs or dipoles, yields a consequent decrease in M .

3. Experimental Results

3.1. DSC Analysis of the HPT-Processed Low-Mo and High-Mo Samples

Fig. 2 shows DSC thermograms taken at a heating rate of 40 K/min for the Low- and High-Mo alloys processed by HPT for 20 turns. The heat flow versus temperature curves were plotted after baseline subtraction. The baseline was determined from a second heating experiment. It is noted that for the Low-Mo alloy the DSC trace displays an endothermic trend at about 627 K due to the Curie transition from a ferromagnetic to a paramagnetic state. This endothermic peak was also observed in the second DSC scan, therefore after the subtraction of the signal of the Curie transition. For the High-Mo alloy, the endothermic peak of the ferromagnetic to paramagnetic transition was not observed. This is in line with former studies (for example, Ref. [34]) which indicated that ~ 5 at.% Mo alloying led to a considerable reduction in the Curie temperature to 333 K, so that the paramagnetic transition cannot be observed in the present experiments starting at 300 K due to the transient DSC signal at the beginning of the measurements.

Fig. 2 shows that for the Low-Mo sample there was a single exothermic DSC peak with a long tail part at the left side of the peak.

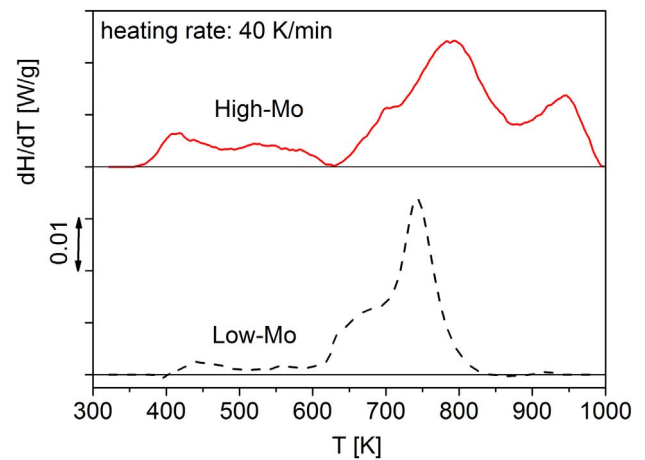


Fig. 2. DSC thermograms obtained at a heating rate of 40 K/min for the HPT-processed Low- and High-Mo alloys.

Between ~ 400 and ~ 600 K only a weak exothermic signal was detected. The majority of the peak appeared between ~ 600 and ~ 830 K. The exothermic peak has a shoulder at the left side and its maximum was observed at a temperature of ~ 743 K. For the High-Mo specimen, between ~ 360 and ~ 630 K the exothermic signal was weak while in the temperature range of 630–1000 K two main exothermic DSC peaks were detected. The first peak was observed between ~ 630 and ~ 875 K while the second peak evolved between ~ 875 K and ~ 1000 K. The peak maxima for these two peaks were found at ~ 786 K and ~ 946 K. Such exothermic peaks are usually related to the recovery and recrystallization of the SPD-processed microstructures. Therefore, it may be concluded that the increase in Mo content resulted in a shift of the exothermic signal to higher temperatures, and thus the Mo alloying improved the stability of the UFG microstructures in Ni. In order to reveal the processes related to the exothermic peaks, the microstructure evolution was studied as a function of annealing temperature and the results are presented in the next sections.

3.2. Microstructure Evolution During Annealing

The XRD patterns indicated that both HPT-processed alloys were single phase fcc solid solutions (see Fig. 1). The lattice parameters for Low-Mo and High-Mo alloys were obtained from the diffraction peak positions as 0.3527 ± 0.0002 and 0.3549 ± 0.0002 nm, respectively. These values are in good agreement with the lattice constants calculated from the chemical compositions of the alloys as shown in a recent report [25]. As the equilibrium solubility limit of Mo in Ni is ~ 0.6 at.% at RT, the HPT-processed High-Mo alloy is a supersaturated solid solution. The phase compositions and the lattice parameters for both alloys remained unchanged during DSC annealing up to 1000 K.

Fig. 3 shows the evolution of the dislocation density as a function of the annealing temperature together with the DSC curves for both alloys. Before annealing, the dislocation density values were $\sim 27 \times 10^{14} \text{ m}^{-2}$ and $\sim 59 \times 10^{14} \text{ m}^{-2}$ in the HPT-processed Low-Mo and High-Mo alloys, respectively. The more than two times larger dislocation density in the High-Mo material is attributed to the hindering effect of Mo solute atoms on the annihilation of dislocations during HPT processing. The heat treatment of the samples led to a gradual reduction in the dislocation density with increasing annealing temperature. For both samples, the dislocation density decreased by about 30–40% up to the onset of the large exothermic DSC peaks at 600–630 K. For the Low-Mo sample, at the end of the exothermic DSC peak at ~ 830 K the dislocation density fell below the detection limit of the present XPLA method ($\sim 10^{13} \text{ m}^{-2}$), thereby suggesting the completion of recovery in the microstructure. For the High-Mo material, the dislocation density decreased to $\sim 20 \times 10^{14} \text{ m}^{-2}$ after the first DSC peak at ~ 875 K,

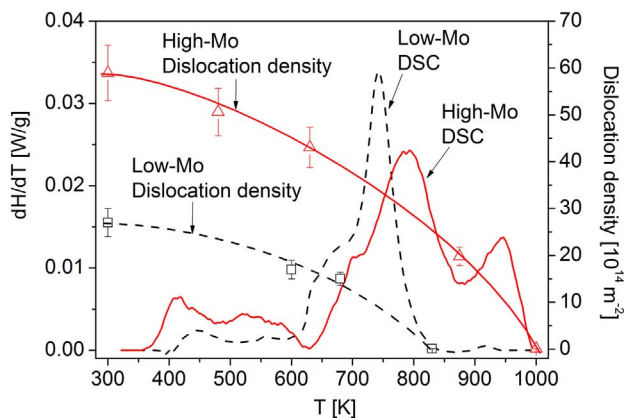


Fig. 3. The average dislocation density obtained by XPLA as function of annealing temperature for the HPT-processed Low- and High-Mo alloys. The corresponding DSC thermograms are also shown in the figure.

thereby indicating a partial recovery of the microstructure. The value of the dislocation density reduced further with increasing annealing temperature and reached a value below $\sim 10^{13} \text{ m}^{-2}$ at the end of the second exothermic DSC peak at $\sim 1000 \text{ K}$.

It is shown in Fig. 4 that, in addition to the reduction of the dislocation density, the dislocation arrangement parameter decreases continuously with increasing annealing temperature. The reduction of the value of M indicates a higher shielding of the strain field of dislocations which suggests their arrangement into low energy configurations such as LAGBs and/or dipolar dislocation walls. Therefore, in both alloys during the recovery of the UFG microstructures there are simultaneous annihilations and clustering of dislocations.

Fig. 5 shows inverse pole figure (IPF) maps obtained on the HPT-processed Low-Mo sample and the specimens annealed at two characteristic temperatures of the DSC thermogram (~ 680 and 830 K). The grain size values determined from the IPF maps are plotted for the Low-Mo sample in Fig. 6 as a function of the annealing temperature. Immediately after HPT processing, the average size of the grains in the Low-Mo specimen was $\sim 184 \text{ nm}$. The grain size remained practically unchanged up to $\sim 680 \text{ K}$ where this corresponds to the beginning of the high exothermic signal in the DSC peak. Thereafter, the grain size quickly increased from ~ 180 to $\sim 874 \text{ nm}$. In addition, Fig. 5c reveals that most of the grains have straight grain boundaries. These observations suggest that the high exothermic signal observed at the end of the DSC peak is related to the recrystallization of the UFG microstructure in the Low-Mo alloy.

The IPF maps in Fig. 7 show the HPT-processed microstructure in

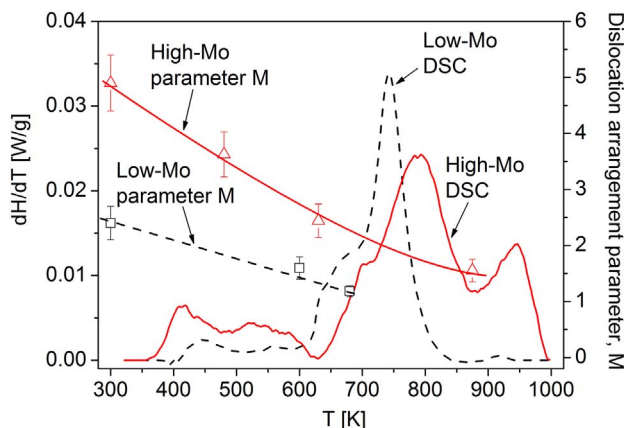


Fig. 4. The dislocation arrangement parameter obtained by XPLA as function of annealing temperature for the HPT-processed Low- and High-Mo alloys. The corresponding DSC thermograms are also shown in the figure.

the High-Mo alloy and also after annealing up to the characteristic temperatures of the DSC thermogram (~ 630 , 875 and 1000 K). The grain sizes determined from the IPF maps are shown in Fig. 6 together with the corresponding DSC curve. Immediately after HPT, the grain size was $\sim 130 \text{ nm}$ and remained unchanged within experimental error up to $\sim 730 \text{ K}$. This temperature corresponds to the end of the shoulder at the left side of the first large DSC peak. When the temperature increased up to the end of the first large exothermic peak at $\sim 875 \text{ K}$, the grain size increased moderately from ~ 130 to $\sim 225 \text{ nm}$. During the second exothermic peak between ~ 875 and $\sim 1000 \text{ K}$, there was a further increase in grain size to $\sim 305 \text{ nm}$ in the High-Mo alloy. After annealing up to $\sim 1000 \text{ K}$ many of the boundaries seem to be straight (for example, in Fig. 7d) but nevertheless a considerable fraction of boundaries is curved which suggests that complete recrystallization does not occur even at the end of the thermogram.

The fraction of LAGBs was also determined from the EBSD data for the HPT-processed and the annealed Low-Mo and High-Mo specimens and plotted as a function of temperature in Fig. 8. After HPT, the LAGB fraction was $\sim 24\%$ for both alloys. First, the LAGB fraction increased with increasing temperature to about 40% which can be attributed to the arrangement of dislocations into LAGBs within the grains in the first stage of recovery of the HPT-processed microstructures. This trend was observed up to temperatures of ~ 650 and $\sim 875 \text{ K}$ for the Low- and High-Mo samples, respectively. Thereafter, the fraction of LAGBs decreased to $\sim 10\%$ for both samples since the dislocations arranged into LAGBs were annihilated during recrystallization.

4. Discussion

This study reveals that both Low-Mo and High-Mo alloys processed by HPT remain a single phase fcc Ni-Mo solid solution during annealing up to 1000 K . For the Low-Mo alloy, this observation is in accordance with the equilibrium phase diagram [35]. At the same time, for the High-Mo alloy the phase diagram suggests that a two-phase microstructure with fcc Ni(Mo) solid solution and tetragonal Ni_5Mo intermetallic compound is stable between ~ 300 and $\sim 500 \text{ K}$. In the temperature range of 500 – 700 K , the phase diagram predicts a microstructure with fcc Ni(Mo) solid solution and tetragonal Ni_4Mo intermetallic compound. Above $\sim 700 \text{ K}$, the single-phase fcc Ni(Mo) solid solution is stable. The lack of transformation from fcc solid solution to a two-phase system below $\sim 700 \text{ K}$ can be explained by the short term of the present DSC annealing process. In addition, a large amount of Mo may be segregated at the grain boundaries, and this may stabilize the microstructure against recrystallization or phase transformation as revealed by former studies [36–38]. The segregation of alloying elements at grain boundaries may lower the grain boundary energy thereby reducing the thermodynamic driving force for recrystallization. In addition, the decrease of the grain boundary energy due to segregation hinders the nucleation of the intermetallic compound as the higher alloying element content in the precipitates must be supplied by the solute atoms at the grain boundaries. In accordance with the present study, a recent investigation also showed the absence of precipitation in nanocrystalline Ni-Mo alloys with different Mo contents up to $21.5 \text{ at.}\%$ annealed at various temperatures up to 1173 K for 1 h [39].

The higher Mo content in the Ni alloy yielded a smaller grain size and a higher dislocation density after HPT processing. This is explained by the retarding effect of solute Mo atoms on the dynamic annihilation of dislocations and the recrystallization during SPD straining. At the same time, the higher dislocation density in the High-Mo alloy led to a larger driving force for recovery and recrystallization. The former kinetic and the latter thermodynamic effects hinder and promote the annihilation of dislocations, respectively. It seems that the increase of the Mo content from 0.28% to 5.04% has a similar influence on these two effects at the beginning of DSC annealing as the recovery started at about 400 K for both alloys as revealed by the DSC thermograms in

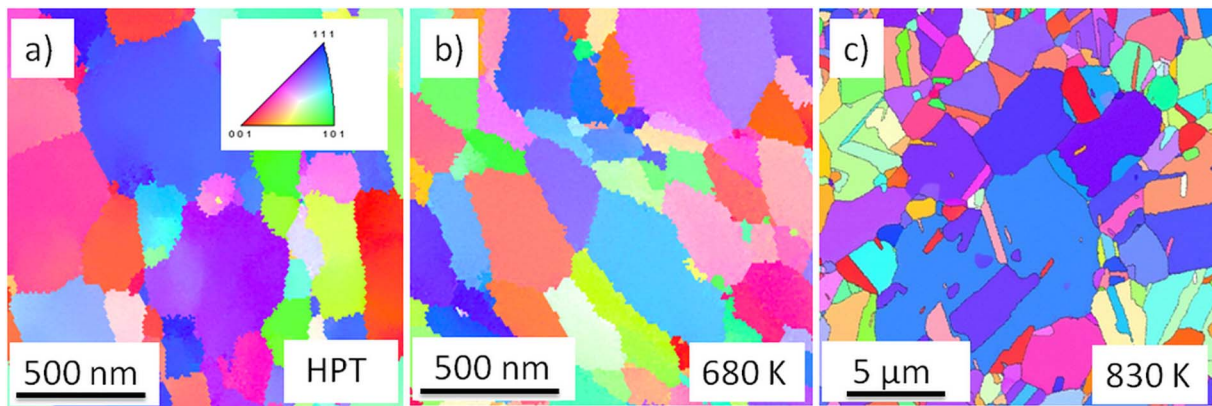


Fig. 5. IPF maps showing the grain structure for the Low-Mo alloy after (a) HPT, (b) subsequent annealing at ~ 680 K and (c) ~ 830 K. The color code for the maps is shown in the inset in (a). The HAGBs are indicated by black lines. (For interpretation of the references to color in this figure legend, the reader is referred to the web version of this article.)

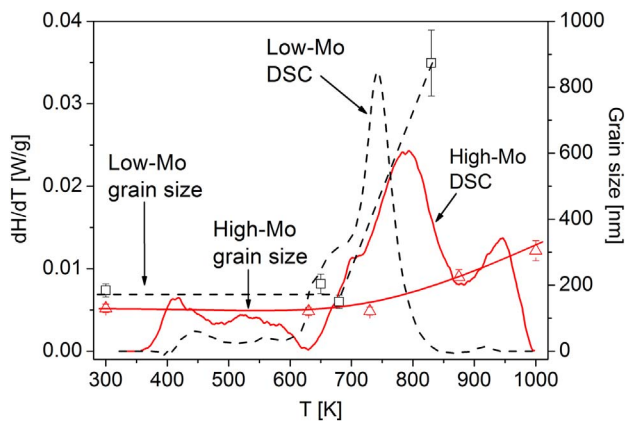


Fig. 6. The average grain size determined by EBSD as function of annealing temperature for the HPT-processed Low- and High-Mo alloys. The corresponding DSC thermograms are also shown in the figure.

Fig. 2. In addition, between ~ 400 and ~ 600 K the relative change of the dislocation density due to recovery was practically the same (about 30–40%) for both alloys. At the same time, the recrystallization occurred at a much higher temperature and the exothermic DSC signal finished later for the High-Mo sample than for the Low-Mo alloy (see Fig. 2). The grain growth during the DSC scan was also less pronounced in the High-Mo material. Thus, it can be concluded that, although the recovery started at similar temperatures for both alloys, the recrystallization occurred at a higher temperature for the High-Mo alloy so that the higher Mo content yielded a considerable increase in the thermal stability of the UFG microstructure. It is noted that the annihilation of vacancy clusters and/or very small dislocation loops during annealing may also contribute to the released heat measured by DSC.

The grain-growth in both alloys was preceded by a reduction in the dislocation density to about one-half of the value measured after HPT and the arrangement of the remaining dislocations into LAGBs as revealed by the decrease of the dislocation arrangement parameter (M) and the increase of the LAGB fraction (see Figs. 4 and 8). When grain growth began, the fraction of LAGBs started to decrease with a concomitant reduction of the dislocation density to practically a zero value. These observations suggest that, in addition to recovery processes, recrystallization also occurred in the temperature ranges of 680–830 K and 875–1000 K for the Low- and High-Mo alloys, respectively. The higher thermal stability of the High-Mo material against recrystallization can be explained by the segregation of Mo solute atoms in the grain boundaries which yields both kinetic and thermodynamic retardation of the grain growth, as discussed in the previous paragraphs. In the Low-Mo alloy annealed up to the end of the exothermic peak at ~ 830 K, the majority of HAGBs are straight which suggests

complete recrystallization. At the same time, for the High-Mo alloy the grain size is much smaller and many curved grain boundaries were detected in the EBSD images, suggesting that only partial recrystallization occurred in this material. Thus, at the heating rate of 40 K/min full recrystallization can be achieved only at temperatures higher than 1000 K which is above the upper temperature limit of the present DSC facility.

The changes in the microstructures of the HPT-processed Low- and High-Mo alloys during annealing are also reflected in the KAM maps shown in Figs. 9 and 10, respectively. These maps were made on the same areas as those shown in the IPF images of Figs. 5 and 7 with the HAGBs indicated by black lines. For all HPT-processed or annealed samples, more than 95% of the pixels inside the grains have local misorientations smaller than 5° . Therefore, the KAM maps were prepared for the misorientation angle range between 0 and 5° . The color codes for the different misorientation angles are shown in the inset of Fig. 9a. The pixels with local misorientations larger than 5° received the same red color as the pixels with the misorientation of 5° . The KAM maps are indicative of local strains in the studied microstructures. Fig. 9a reveals an inhomogeneous spatial distribution of distortion inside the grains for the Low-Mo alloy processed by HPT. It is noted that, although in some regions low KAM values were observed as indicated by blue color, they may contain high dislocation densities as the statistically stored dislocations are not arranged into LAGBs and therefore they do not cause local misorientations in the KAM maps. Indeed, XPLA indicated a high dislocation density ($\sim 27 \times 10^{14} \text{ m}^{-2}$) in the HPT-processed Low-Mo alloy. Until the grain size remained practically unchanged (up to ~ 680 K), large local misorientation angle values were detected in the KAM maps (see Fig. 9b). At the same time, between ~ 680 K and ~ 830 K the large exothermic signal and the extensive grain growth were accompanied by a strong reduction of the KAM values inside the grains. Considerable local misorientations may be observed only in the vicinity of some grain boundaries. These HAGBs are assumed to be incoherent or semicoherent boundaries with significant lattice distortions. However, the majority of HAGBs are straight without considerable KAM values in the neighboring areas. These boundaries are assumed to be coherent HAGBs formed during recrystallization.

Fig. 10a reveals significant misorientations within the grains for the HPT-processed High-Mo alloy. High KAM values were also observed in the samples annealed up to the beginning (~ 630 K) and the end (~ 875 K) of the first large exothermic DSC peak, as shown in Figs. 10b and c, respectively. This observation suggests that considerable recrystallization does not occur in the High-Mo alloy between ~ 630 and ~ 875 K even if the average grain size increased from ~ 130 nm to ~ 225 nm. Therefore, the first large exothermic peak is related mainly to the recovery of the microstructure which is accompanied by moderate grain growth. During the second large DSC peak

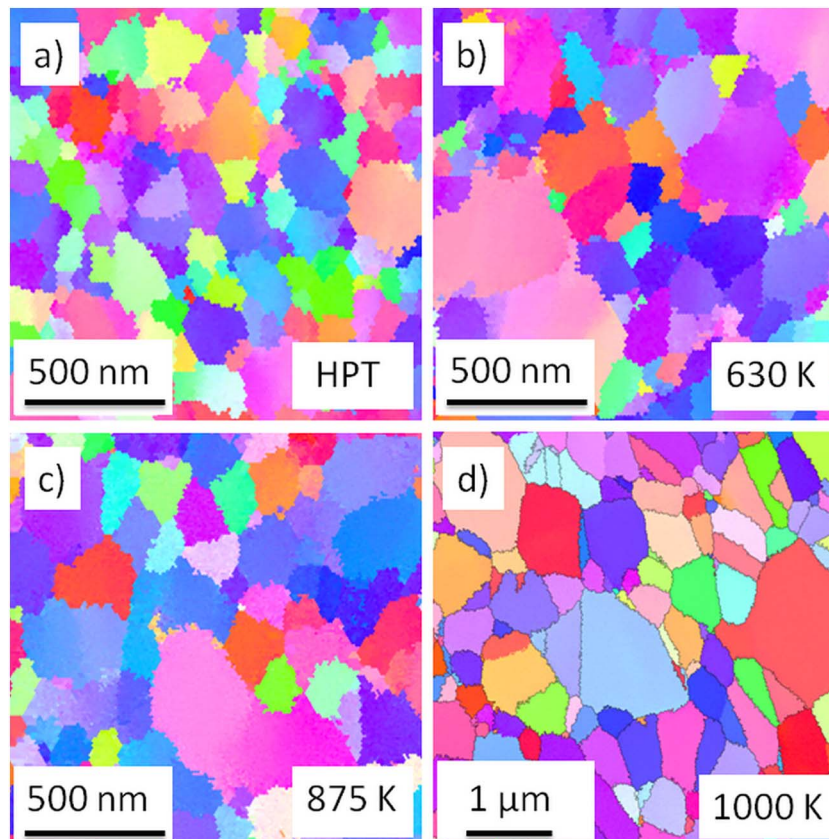


Fig. 7. IPF maps showing the grain structure for the High-Mo alloy after (a) HPT, (b) subsequent annealing at ~630 K, (c) ~875 K and (d) ~1000 K. The color code for the maps is shown in the inset in Fig. 5a. The HAGBs are indicated by black lines. (For interpretation of the references to color in this figure legend, the reader is referred to the web version of this article.)

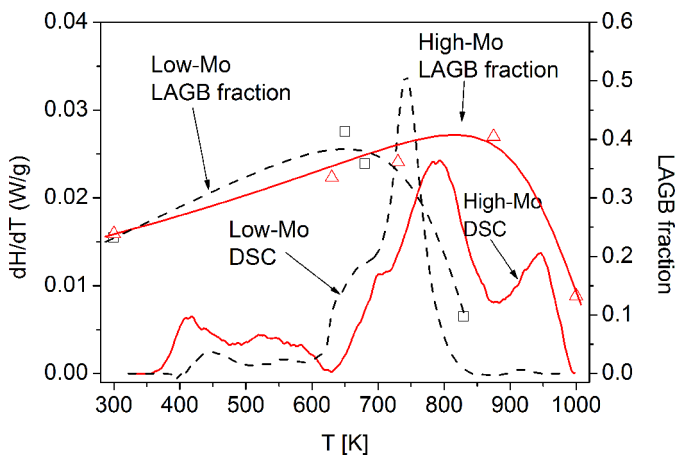


Fig. 8. The LAGB fraction determined by EBSD as function of annealing temperature for the HPT-processed Low- and High-Mo alloys. The corresponding DSC thermograms are also shown in the figure.

the misorientations inside the grains were strongly reduced and considerable KAM values are only observed in the vicinity of HAGBs. In addition, there are many grain boundaries which are straight and free of significant KAM values. It is assumed that these HAGBs are formed by recrystallization. The fraction of the distortion-free grain boundaries among HAGBs is lower for the High-Mo alloy than for the Low-Mo sample (compare Figs. 9c and 10d) which suggests that recrystallization in the High-Mo material was not complete up to 1000 K. This observation is supported by the moderate grain growth to ~305 nm. Therefore, it is concluded that the increase of Mo content in Ni has a stronger retardation effect on the recrystallization than on the recovery. The latter process started at about 400 K for both alloys

while the onset temperature of recrystallization was shifted from ~680 to ~875 K when the Mo concentration increased from ~0.28 to ~5.04 at.%. This difference is explained by the segregation of Mo atoms at HAGBs which hinders grain growth during recrystallization.

The more pronounced separation of recovery and recrystallization for the High-Mo alloy led to two large DSC peaks between ~630 and ~1000 K (see Fig. 2). It should be noted that the separation of the recovery and recrystallization (or grain-growth) processes into two DSC peaks was also observed for severely deformed Al-based solid solutions either in powder or bulk form [23,24]. In addition, two exothermic peaks were detected for UFG Cu consolidated from a coarse-grained powder using the HPT technique [40]. In this case, contamination on the powder surface may be segregated at the grain boundaries in the sintered UFG sample which hinders grain boundary motion during recrystallization and grain growth.

5. Summary and Conclusions

1. The influence of Mo alloying on the evolution of microstructure during annealing of UFG Ni was studied. UFG microstructures with high dislocation density were achieved by the consecutive application of cryorolling and HPT at RT for 20 turns. The grain sizes for the alloys with low (~0.28 at.%) and high (~5.04 at.%) Mo concentrations were ~184 and ~130 nm, respectively, at the peripheral regions of the HPT disks. The dislocation density for the higher Mo content was more than two times larger ($\sim 59 \times 10^{14} \text{ m}^{-2}$) than for the lower Mo concentration ($\sim 27 \times 10^{14} \text{ m}^{-2}$). Recovery and recrystallization processes in the two UFG Ni alloys were investigated by DSC in the temperature range between 300 and 1000 K.
2. For both the Low- and High-Mo alloys, the recovery of the microstructure started at about 400 K as revealed by the moderate exothermic DSC signal and the decrease of the dislocation density.

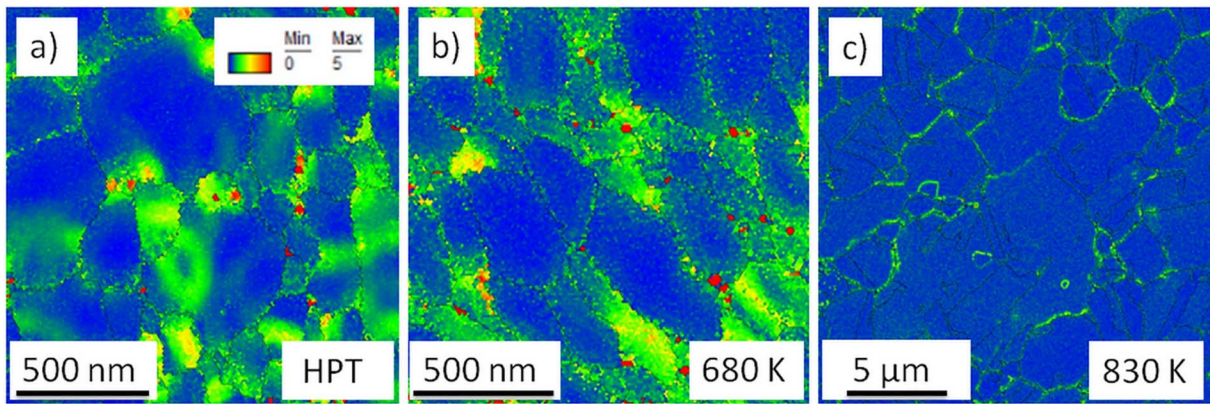


Fig. 9. KAM images showing the local misorientations between 0 and 5° for the Low-Mo alloy after (a) HPT, (b) subsequent annealing at ~680 K and (c) ~830 K. The color code for the maps is shown in the inset in (a). The HAGBs are indicated by black lines. (For interpretation of the references to color in this figure legend, the reader is referred to the web version of this article.)

The negligible effect of the higher Mo content on the onset temperature of recovery is explained by the compensation of the higher thermodynamic driving force for recovery due to the higher defect (e.g., dislocation) density by the stronger kinetic retardation of the lattice defect annihilation due to the higher Mo concentration. When only recovery occurred in both alloys (between ~400 and ~600 K), the relative change of the dislocation density was practically the same. An accelerated reduction of the dislocation density was observed when recrystallization started.

3. During recovery, the decrease of the dislocation density is accompanied by an increase in the fraction of LAGBs since the remaining dislocations are arranged into low-energy configurations, such as LAGBs. This is also reflected in the decrease of the dislocation

arrangement parameter determined by XLP. The temperature range of the recovery is much larger for the High-Mo alloy (~515 K) than for the Low-Mo sample (~280 K).

4. According to the DSC thermograms and the microstructure investigations, the recrystallization in the Low- and High-Mo alloys starts at about 680 and 875 K, respectively. The much higher onset temperature of recrystallization for the High-Mo alloy is due to the segregation of solute Mo atoms at the grain boundaries which may reduce the grain boundary energy and additionally hinders the motion of the grain boundaries. It appears that Mo alloying has a more pronounced effect on recrystallization than on the recovery processes.
5. The strong influence of the solute Mo atoms on recrystallization was

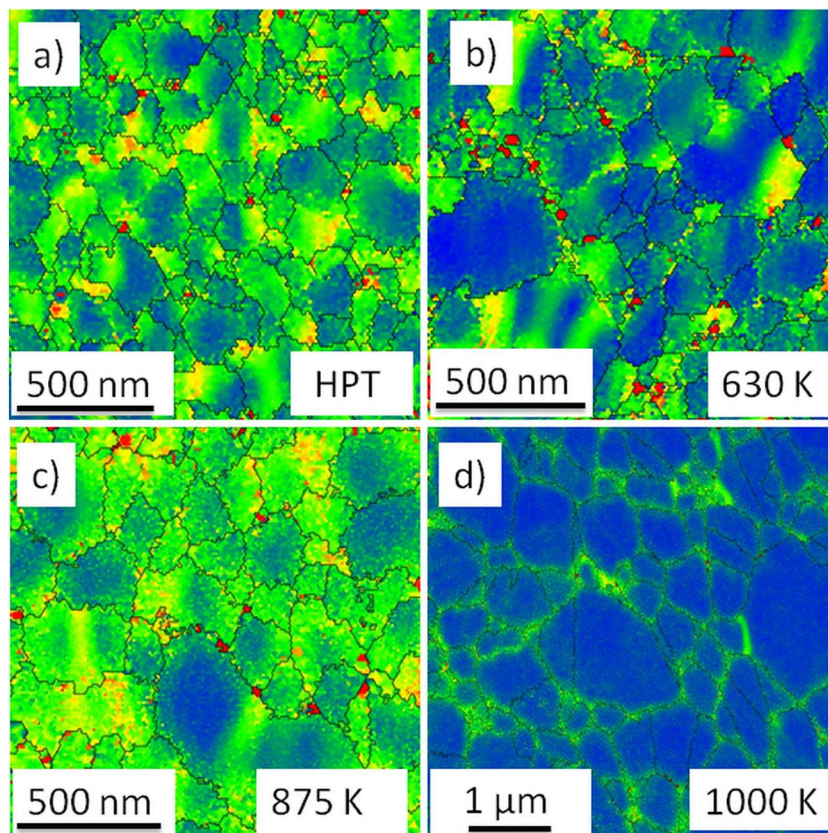


Fig. 10. KAM images showing the local misorientations between 0 and 5° for the High-Mo alloy after (a) HPT, (b) subsequent annealing at ~630 K, (c) ~875 K and (d) ~1000 K. The color code for the maps is shown in the inset in Fig. 9a. The HAGBs are indicated by black lines. (For interpretation of the references to color in this figure legend, the reader is referred to the web version of this article.)

also reflected in the DSC thermograms. For the Low-Mo alloy, the heat released due to recovery cannot be separated from the exothermic signal caused by recrystallization. At the same time, for the High-Mo material a separate DSC peak was detected during recrystallization although this peak strongly overlapped with the exothermic peak for recovery. The KAM maps revealed that at the highest temperature of annealing (~1000 K) the Low-Mo alloy contains a higher fraction of straight and distortion-free HAGBs than the High-Mo material. In addition, the grain size in the latter sample was much smaller (~305 nm) than in the Low-Mo sample (~874 nm) after annealing at ~1000 K. Therefore, it is concluded that the higher Mo content significantly increases the stability of the SPD-processed UFG microstructure in Ni.

Acknowledgements

This work was supported by the Hungarian Scientific Research Fund, OTKA, Grant no. K-109021. The authors are grateful to Mr. Alajos Ö. Kovács and Mr. Gábor Varga for the DSC and EBSD investigations, respectively. Two of the authors were supported by the European Research Council under ERC Grant Agreement No. 267464-SPDMETALS (YH and TGL).

References

- R.Z. Valiev, I. Sabirov, A.P. Zhilyaev, T.G. Langdon, Bulk nanostructured metals for innovative applications, *JOM* 64 (2012) 1134–1142.
- R.Z. Valiev, A.P. Zhilyaev, T.G. Langdon, *Bulk Nanostructured Materials: Fundamentals and Applications*, first ed., John Wiley & Sons Inc, Hoboken, NJ, 2014.
- R.Z. Valiev, Y. Estrin, Z. Horita, T.G. Langdon, M.J. Zehetbauer, Y. Zhu, Producing bulk ultrafine-grained materials by severe plastic deformation: ten years later, *JOM* 68 (2016) 1216–1226.
- A.P. Zhilyaev, T.G. Langdon, Using high-pressure torsion for metal processing: fundamentals and applications, *Prog. Mater. Sci.* 53 (2008) 893–979.
- J. Gubicza, 2nd and extended edition (Ed.), *Defect Structure and Properties of Nanomaterials*, Woodhead Publishing, Duxford, UK, 2017.
- J. Gubicza, S.V. Dobatkin, E. Khosravi, A.A. Kuznetsov, J.L. Lábár, Microstructural stability of Cu processed by different routes of severe plastic deformation, *Mater. Sci. Eng. A* 528 (2011) 1828–1832.
- A. Alhamidi, K. Edalati, Z. Horita, S. Hirose, K. Matsuda, D. Terada, Softening by severe plastic deformation and hardening by annealing of aluminum–zinc alloy: significance of elemental and spinodal decompositions, *Mater. Sci. Eng. A* 610 (2014) 17–27.
- O. Andreau, J. Gubicza, N.X. Zhang, Y. Huang, P. Jenei, T.G. Langdon, Effect of short-term annealing on the microstructures and flow properties of an Al-1% Mg alloy processed by high-pressure torsion, *Mater. Sci. Eng. A* 615 (2014) 231–239.
- A. Bachmaier, A. Hohenwarter, R. Pippan, New procedure to generate stable nanocrystallites by severe plastic deformation, *Scr. Mater.* 61 (2009) 1016–1019.
- D. Setman, M.B. Kerber, E. Schafner, M.J. Zehetbauer, Activation enthalpies of deformation-induced lattice defects in severe plastic deformation nanometals measured by differential scanning calorimetry, *Metall. Mater. Trans. A* 41 (2010) 810–815.
- A.P. Zhilyaev, G.V. Nurislamova, S. Surinach, M.D. Baró, T.G. Langdon, Calorimetric measurements of grain growth in ultrafine-grained nickel, *Mater. Phys. Mech.* 5 (2002) 23–30.
- N. Lugo, N. Llorca, J.J. Sunol, J.M. Cabrera, Thermal stability of ultrafine grains size of pure copper obtained by equal-channel angular pressing, *J. Mater. Sci.* 45 (2010) 2264–2273.
- W.Q. Cao, C.F. Gu, E.V. Pereloma, C.H.J. Davies, Stored energy, vacancies and thermal stability of ultrafine grained copper, *Mater. Sci. Eng. A* 492 (2008) 74–79.
- J. Cizek, I. Prochazka, M. Cieslar, R. Kuzel, J. Kuriplach, F. Chmelik, I. Stulikova, F. Becvar, O. Melikhova, Thermal stability of ultrafine grained copper, *Phys. Rev. B* 65 (2002) 094106.
- Y.K. Huang, A.A. Menovsky, F.R. de Boer, Calorimetric analysis of the grain growth in nanocrystalline copper samples, *Nanostruct. Mater.* 2 (1993) 587–595.
- A. Kumpmann, B. Günther, H.-D. Kunze, Thermal stability of ultrafine-grained metals and alloys, *Mater. Sci. Eng. A* 168 (1993) 165–169.
- Z. Hegedűs, J. Gubicza, M. Kawasaki, N.Q. Chinh, K. Stüvegh, Zsolt Fogarassy, T.G. Langdon, High temperature thermal stability of ultrafine-grained silver processed by equal-channel angular pressing, *J. Mater. Sci.* 48 (2013) 1675–1684.
- J. Lian, R.Z. Valiev, B. Baudelet, On the enhanced grain growth in ultrafine grained metals, *Acta Metall. Mater.* 43 (1995) 4165–4170.
- S.C. Tjong, H. Chen, Nanocrystalline materials and coatings, *Mater. Sci. Eng. R* 45 (2004) 1–88.
- C.M. Kuo, C.S. Lin, Static recovery activation energy of pure copper at room temperature, *Scr. Mater.* 57 (2007) 667–670.
- S. Divinski, J. Ribbe, G. Schmitz, C. Herzog, Grain boundary diffusion and segregation of Ni in Cu, *Acta Mater.* 55 (2007) 3337–3346.
- D. Setman, E. Schafner, E. Korznikova, M.J. Zehetbauer, The presence and nature of vacancy type defects in nanometals obtained by severe plastic deformation, *Mater. Sci. Eng. A* 493 (2008) 116–122.
- F. Zhou, X.Z. Liao, Y.T. Zhu, S. Dallek, E.J. Lavernia, Microstructural evolution during recovery and recrystallization of a nanocrystalline Al-Mg alloy prepared by cryogenic ball milling, *Acta Mater.* 51 (2003) 2777–2791.
- B. Adamczyk-Cieslak, J. Mizera, K.J. Kurzydowski, Thermal stability of model Al-Li alloys after severe plastic deformation – effect of the solute Li atoms, *Mater. Sci. Eng. A* 527 (2010) 4716–4722.
- G. Kapoor, Y. Huang, V.S. Sarma, T.G. Langdon, J. Gubicza, Effect of Mo addition on the microstructure and hardness of ultrafine-grained Ni alloys processed by a combination of cryorolling and high-pressure torsion, *Mater. Sci. Eng. A* 688 (2017) 92–100.
- E.B. Lehman, A. Bigos, P. Indyka, M. Kot, Electrodeposition and characterization of nanocrystalline Ni-Mo coatings, *Surf. Coat. Technol.* 211 (2011) 67–71.
- J. Eickemeyer, D. Selbmann, R. Opitz, B. de Boer, B. Holzapfel, L. Schultz, U. Miller, Nickel-refractory metal substrate tapes with high cube texture stability, *Supercond. Sci. Technol.* 14 (2001) 152–159.
- D.E. Brown, M.N. Mahmood, M.C.M. Man, A.K. Turner, Preparation and characterization of low overvoltage transition metal alloy electrocatalysts for hydrogen evolution in alkaline solutions, *Electrochim. Acta* 29 (1984) 1551–1556.
- R. Schulz, J.Y. Huot, M.L. Trudeau, L.D. Bailey, Z.H. Yan, S. Jin, et al., Nanocrystalline Ni-Mo alloys and their application in electrocatalysis, *J. Mater. Res.* 9 (1994) 2998–3008.
- J.R. McKone, B.R. Sadtler, C.A. Werlang, N.S. Lewis, H.B. Gray, Ni – Mo nanoparticles for efficient electrochemical hydrogen evolution, *ACS Catal.* 3 (2013) 166–169.
- R.B. Figueiredo, P.R. Cetlin, T.G. Langdon, Using finite element modeling to examine the flow processes in quasi-constrained high-pressure torsion, *Mater. Sci. Eng. A* 528 (2011) 8198–8204.
- J. Nelson, D. Riley, An experimental investigation of extrapolation methods in the derivation of accurate unit-cell dimensions of crystals, *Proc. Phys. Soc. Lond.* 57 (1945) 160–177.
- G. Ribárik, J. Gubicza, T. Ungár, Correlation between strength and microstructure of ball-milled Al–Mg alloys determined by X-ray diffraction, *Mater. Sci. Eng. A* 387–389 (2004) 343–347.
- M. Karolus, E. Lagiewka, The structural studies on nanocrystalline Ni-Mo alloys after annealing, in: Henryk Morawiec, Danuta Stróz (Eds.), *Proceedings of the XIX Conference of Applied Crystallography*, World Scientific, Singapore, 2004, pp. 337–341.
- S.H. Zhou, Y. Wang, L.Q. Chen, Z.K. Liu, R.E. Napolitano, Solution-based thermodynamic modeling of the Ni–Al–Mo system using first-principles calculations, *Calphad* 46 (2014) 124–133.
- R. Kirchheim, Grain coarsening inhibited by solute segregation, *Acta Mater.* 50 (2002) 413–419.
- F. Liu, R. Kirchheim, Nano-scale grain growth inhibited by reducing grain boundary energy through solute segregation, *J. Cryst. Growth* 264 (2004) 385–391.
- H.A. Murdoch, C.A. Schuh, Stability of binary nanocrystalline alloys against grain growth and phase separation, *Acta Mater.* 61 (2013) 2121–2132.
- J. Hu, Y.N. Shi, X. Sauvage, G. Sha, K. Lu, Grain boundary stability governs hardening and softening in extremely fine nanograined metals, *Science* 355 (2017) 1292–1296.
- P. Jenei, J. Gubicza, E.Y. Yoon, H.S. Kim, J.L. Labar, High temperature thermal stability of pure copper and copper - carbon nanotube composites consolidated by High Pressure Torsion, *Compos. Part A* 51 (2013) 71–79.